

The Spectrum of Fault Slip in Elastoplastic Fault Zones

Md Shumon Mia^{1,2}, Mohamed Abdelmeguid^{2,3}, Ahmed E. Elbanna^{2,4}

¹Department of Mechanical Science and Engineering, University of Illinois at Urbana-Champaign, Urbana, IL, USA.

²Department of Civil and Environmental Engineering, University of Illinois at Urbana-Champaign, Urbana, IL, USA.

³Graduate Aerospace Laboratories, California Institute of Technology, Pasadena, CA, USA.

⁴Beckman Institute of Advanced Science and Technology, University of Illinois at Urbana-Champaign, Urbana, IL, USA.

Corresponding author: Md Shumon Mia (mmia2@illinois.edu)

This is a non-peer reviewed preprint submitted to Earth and Planetary Science Letters.

Highlights:

- Numerical models for inelastic fault zones show that the spectrum of fault slip depends on the bulk yield strength relative to fault reference frictional strength.
- For a given fault friction, weaker fault zones experience more inelastic deformation and plastic dissipation leading to the emergence of a new stability transition boundary that limits earthquake size regardless of fault length.
- As bulk inelastic dissipation increases, fault slip transitions from fast to slow slip and from throughgoing to localized ruptures, and eventually to complete locking of seismogenic patch.

20 **Abstract**

21 Natural faults are usually surrounded by damage zones that exhibit nonlinear material response.
22 This study investigates the role of fault zone strength in modulating the spectrum of fault slip
23 across different spatio-temporal scales. We carry out long-term simulations of seismic and
24 aseismic slip for an elastoplastic spring slider model with rate-and-state friction as well as a
25 continuum model of a 2D anti-plane rate-and-state fault embedded in an elastoplastic bulk. Results
26 of the elastoplastic spring slider model show the emergence of a new stability boundary, depending
27 on the bulk yield strength relative to fault frictional strength, that limits the rupture size regardless
28 of the fault length. Continuum simulations generate a spectrum of slip analogous to the spring
29 slider model including localized or migrating events of slow and fast slip. A fault may remain
30 locked for yield strength sufficiently low and close to fault reference strength even if it is
31 intrinsically rate weakening and larger than the nucleation length scale predicted by the elastic
32 analysis. These findings shed new light on the nature of fault frictional stability and suggest the
33 critical role of the fault zone rheological properties in modulating the spectrum of fault slip.

34 **1. Introduction**

35 Unstable sliding of geologic faults manifests itself as earthquakes—one of the deadliest and most
36 prevalent yet unpredictable natural hazards. Apart from large earthquakes, faults are also found to
37 host small earthquakes, and slow slip events (Beroza & Ide, 2011; Ito et al., 2013; Burgmann
38 2018). Usually, earthquakes are associated with frictional sliding on fault surfaces encompassing
39 long-term slow aseismic slip and rapid seismic ruptures (Avouac 2015). However, fault zone
40 complexities, including geometric and material non-linearity (Ben-Zion & Sammis, 2003; Mitchell
41 & Faulkner, 2009; Lewis & Ben-Zion, 2010), influence the fault slip behavior leading to complex
42 pattern of seismicity in space and time (Chen et al., 2020; Ross et al., 2020). Physics-based

43 simulations for sequence of earthquakes and aseismic slip (Ben-Zion & Rice, 1993; Lapusta et al.,
44 2000; Chen & Lapusta 2009; Kaneko et al., 2010; Barbot et al., 2012; Allison & Dunham, 2021;
45 Erickson et al., 2022; Jiang et al., 2022; Abdelmeguid & Elbanna, 2022a, 2022b) are emerging as
46 promising tools for understanding the complex processes associated with different forms of
47 frictional instabilities and resulting slip pattern, as well as in developing seismic hazard models.

48 Stable and unstable frictional sliding is largely attributed to the frictional properties of the fault
49 whether the steady-state frictional strength increases with slip rate (velocity strengthening) or
50 decreases with slip rate (velocity weakening). A velocity-strengthening patch is generally
51 associated with stable aseismic sliding and may become unstable through enhanced coseismic
52 weakening associated with flash heating or a rapid increase in pore fluid pressure due to shear
53 heating (Noda & Lapusta, 2013). While a fault with velocity weakening friction is locked during
54 the interseismic period, it is potentially unstable and generates different patterns of slip. The style
55 of slip in terms of peak slip rate, spatial extent, and temporal periodicity, depends on the size of
56 the velocity weakening patch relative to the critical length scale associated with nucleation as well
57 as the relative magnitude of frictional parameters associated with static and dynamic stress drop
58 (Barbot 2019; Cattania 2019). Generation of slow slip sequence accompanied by slow earthquakes
59 are shown in Barbot (2019) to depend on the relative magnitude of the frictional parameters and
60 the relative fault size. Specifically, slow slip is found in these studies when the length of the
61 velocity weakening patch is close to the nucleation length.

62 Additionally, geologic heterogeneities (Skarbek et al., 2012; Bedford et al., 2022) in terms of the
63 different proportions of velocity strengthening and velocity weakening patches, as well as the rate-
64 dependent evolution (Kaproth & Marone, 2013) of frictional parameters are possible mechanism
65 for slow slip generation. Velocity-weakening friction generating stick-slip instabilities may

66 generate slow slip when rate-and-state friction parameters evolve with slip rate and take transition
67 from velocity weakening to velocity strengthening. Numerical simulations using a spring-slider
68 model by Im et al. (2020) show that velocity dependent frictional parameters enable generating
69 slow slip events having similar characteristics to those observed in nature (Dragert et al., 2001;
70 Heki & Kataoka, 2008; Radiguet et al., 2012). However, it is not clear what physical mechanism
71 may lead to this rate dependence of the frictional parameters.

72 Pore pressure also plays an important role in controlling spectrum of slip. Fluid pressure reduces
73 effective normal stress and increases the nucleation length scale. Accordingly, the size of the
74 seismogenic velocity weakening patch decreases relative to the size of the nucleation patch. This
75 results in slow slip transients (Liu & Rice, 2007). Dilatant strengthening (Segall et al., 2010),
76 resulting in reduced pore pressure, also explains the generation of slow slip events in a seismogenic
77 velocity-weakening region. Slow and fast slip may arise through the relative contribution of
78 dilatancy-induced strengthening and enhanced coseismic weakening due to thermal pressurization
79 of pore fluid. Dilatant hardening itself may be a manifestation of inelastic processes associated
80 with propagating crack tip (French & Zhu, 2017).

81 These on-fault characteristics controlling the spectrum of slip are investigated mostly with
82 homogeneous elastic bulk. Heterogenous bulk with a low velocity zone near the fault may generate
83 slip complexity (Abdelmeguid 2019; Thakur et al. 2020; Nie & Barbot 2022). Also, a recent study
84 by Collettini et al. (2022) explains the observation of distributed microseismicity through a
85 conceptual model of distributed ductile deformation in the bulk. Incorporation of viscoelastic fault
86 zones (Miyake & Noda, 2019; Goswami & Barbot, 2018) and viscous damping in fault strength
87 (Wu 2021; Nakata et al., 2011) are shown to generate slow slip events. Using numerical simulation
88 with elastoplastic shear zone, Tong & Lavier (2018) shows generation of slow and fast slip events

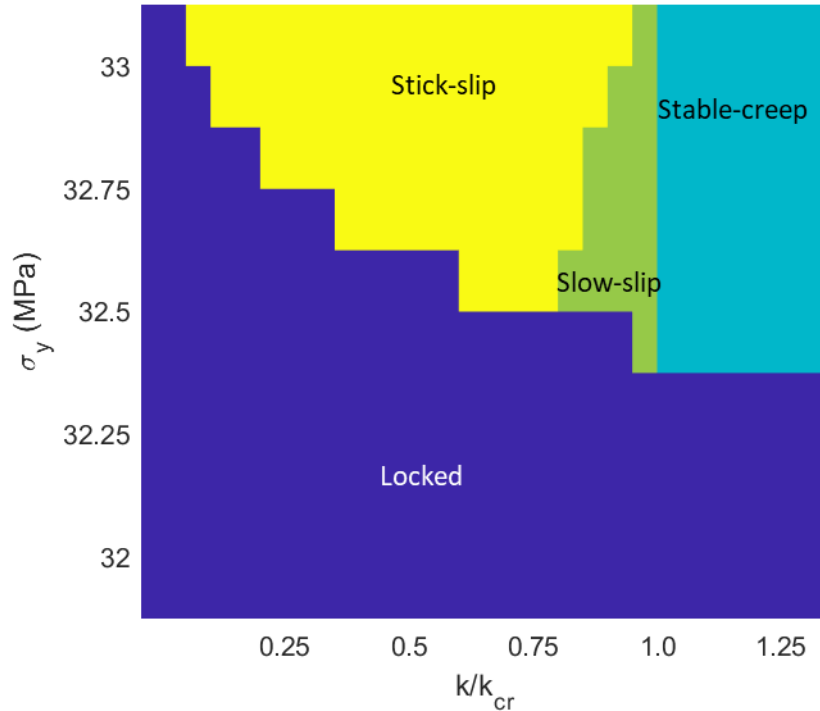
89 by varying the rate-and-state friction parameters. By reducing the difference between the direct
90 effect parameter and state evolution parameter, they found slip pattern to change from fast slip
91 events to slow slip. In the limit of vanishing difference between the friction parameters,
92 corresponding to the limit of velocity neutral, creeping events are found.

93 In our previous work on seismic cycle simulations with off-fault plasticity (Mia et al., 2022), we
94 showed that bulk yield strength and post-yield viscous relaxation contribute to the emergence of
95 spatio-temporal clustering of seismicity. Here, we investigate the effect of off-fault bulk strength
96 on fault slip expanding the parameter space for yield strength to also consider values close to the
97 reference frictional strength. This is a critical parameter regime that have not been investigated
98 before and may qualitatively alter the partitioning of slip and energy dissipation between on-fault
99 and off-fault processes. To that end, we first simulate the long-term frictional sliding of an
100 elastoplastic spring slider model with rate-and-state friction. Then, to further corroborate our
101 findings, we investigate sequences of seismic and aseismic slip on a 2D anti-plane rate and state
102 model embedded in a fully continuum elastoplastic model. We evaluate the resulting slip patterns
103 with a special focus on slow slip.

104 **2. Elastoplastic spring slider**

105 We simulate the long-term sliding of a spring-block system under constant load-point velocity
106 applied at the end of the spring. The frictional interface is velocity weakening governed by rate-
107 and-state friction law (Dieterich, 1979; Ruina, 1983) and the state evolution follows the aging law
108 (Ampuero & Rubin, 2008). The friction law is outlined in the Supplementary Information (Text-
109 S1). To investigate the effect of bulk strength on frictional sliding, we vary the yield strength and
110 the stiffness of the spring. Critical stiffness (Rice & Ruina, 1983; Ranjith & Rice, 1999) is related
111 to the frictional properties and normal stress, and is defined by, $k_{cr} = \sigma_n(b - a)/L$. Critical

112 stiffness marks the transition between stable and unstable frictional sliding in a purely elastic
 113 setting.



114
 115
 116 **Figure 1.** Sliding patterns for an elastoplastic spring block system depending on yield strength and stiffness of the
 117 spring. Reference strength of the frictional interface is $\sigma_n f_o = 30 \text{ MPa}$. Sliding patterns change from stick-slip to
 118 slow-slip as spring stiffness becomes close to a critical stiffness defined for the elastic system from the frictional
 119 parameters as $k_{cr} = \sigma_n(b - a)/L$. For stiffness higher than critical value, the sliding is stable. A region of slow-slip
 120 exists between stick-slip and stable-creep for a narrow range of stiffness and yield strength values. There is another
 121 transition towards lower stiffness, which depends on the magnitude of the yield strength, where the slider remains
 122 locked. This new stability boundary does not exist for purely elastic spring block systems.

123 From stability analysis (Ranjith & Rice, 1999; Rice et al., 2001), it is known that stiffness greater
 124 than the critical value correspond to stable sliding which tends to attain steady state in sync with
 125 the imposed load point velocity. For elastic spring, stiffness lower than the critical value generate
 126 unstable sliding. The elastoplastic spring bock slider shows different sliding patterns ranging from
 127 stick-slip to complete locking depending on the yield strength and the elastic stiffness of the spring
 128 (Figure-1). We classify the slip patterns based on the amplitude of the block's peak slip rate. Slow
 129 slip is identified with slip rate lower than a seismic threshold (taken here to be 0.01 m/s) but

130 higher than the background plate rate (10^{-9} m/s). Stick slip corresponds to slip rate exceeding the
131 seismic threshold. We observe that slow slip emerges for a narrow range of yield strength and
132 stiffness values. The block also creeps stably at the imposed loading rate for stiffness values larger
133 than the critical value predicted by the elastic analysis. However, another new transition boundary
134 emerges with plasticity, in the limit of lower stiffness, that is not observed in purely elastic
135 analysis. This transition from stick-slip to locking (i.e., sliding with slip rates that are orders of
136 magnitudes slower than the imposed plate loading rate) depends on the yield strength. As yield
137 strength decreases, this transition stiffness increases. For sufficiently low yield strength as
138 becomes close to the reference frictional strength ($\sigma_n f_o$), the slip rate asymptotically decreases to
139 $\sim 10^{-15}$ m/s, orders of magnitude lower than the imposed plate rate. We refer to the sliding with
140 this negligible slip rate as locked.

141 **3. Continuum simulation of a 2D anti-plane rate-and-state fault**

142 We model a 2D anti-plane rate-and-state fault embedded in a full-space elastoplastic medium
143 subjected to slow tectonic plate rate. The fault has a central velocity-weakening VW region
144 surrounded by velocity-strengthening VS patches from both sides. Off-fault material response is
145 modeled with J2 plasticity which coincides with Drucker-Prager plasticity for the anti-plane setting
146 with no variation in normal stress. A hybrid scheme combining finite element and spectral
147 boundary integral is employed for spatial discretization (Abdelmeguid et al., 2019; Mia et al.,
148 2022; Abdelmeguid & Elbanna 2022b). We use an adaptive time-stepping algorithm (Lapusta et
149 al. 2000) to efficiently resolve slow and fast slip. The model geometry with the hybrid scheme
150 setup as well as the input parameters for the simulations are outlined in the Supplementary
151 Information (Text-S2, Table-S1, Figure-S1).

152 We simulate sequences of earthquakes and aseismic slip (SEAS) with different values of yield
153 strength to investigate the effect of bulk strength on long-term fast and slow slip. Resulting
154 patterns, given as space-time contours of the fault slip rate, with different values of yield strength
155 are shown in Figure 2. The temporal evolution of the peak slip rate in different cases is shown in
156 Supplementary Information, Figure-S2. The simulations show sliding patterns analogous to the
157 elastoplastic spring slider model. For lower yield strength the fault remains locked without
158 generating any seismic event. When the yield strength is increased, the fault generates unstable
159 frictional sliding including slow slip, spatially localized seismic events, and partial ruptures
160 distributed over the fault length intermixed with transient episodes of slow slip. For higher values
161 of yield strength, or in the limit of purely elastic bulk, the fault fails in predominantly large, fault-
162 spanning, fast earthquakes. Below we briefly describe these different slip regimes.

163 **Locked fault:** When the yield strength (31 MPa) is close to the fault reference frictional strength
164 ($\sigma_n f_o = 30$ MPa), the slip rate of the central VW patch decreases to $\sim 10^{-15}$ m/s (Figure-2a).
165 Relative to the plate loading rate, this slip rate is orders of magnitude smaller which indicates that
166 the seismogenic zone (VW patch) of the fault remains effectively locked or stuck. The VS patch
167 of the fault creeps following the plate loading. Aseismic creep from the VS patch penetrates
168 slightly into the VW patch but the peak slip rate remains close to the imposed plate rate (10^{-9} m/s)
169 in a very limited region adjacent to the VS patch as shown in Figure-2a and Supplementary
170 Information, Figure-S2a.

171 **Slow slip:** When the yield strength is increased to 32 MPa, slow slip emerges (Figure-2b, 2g, 2j).
172 Signature of creep penetration exists near the transition between the VS and VW patches. The
173 duration of the slow slip events for yield strength 32 MPa is in the scale of weeks to month.

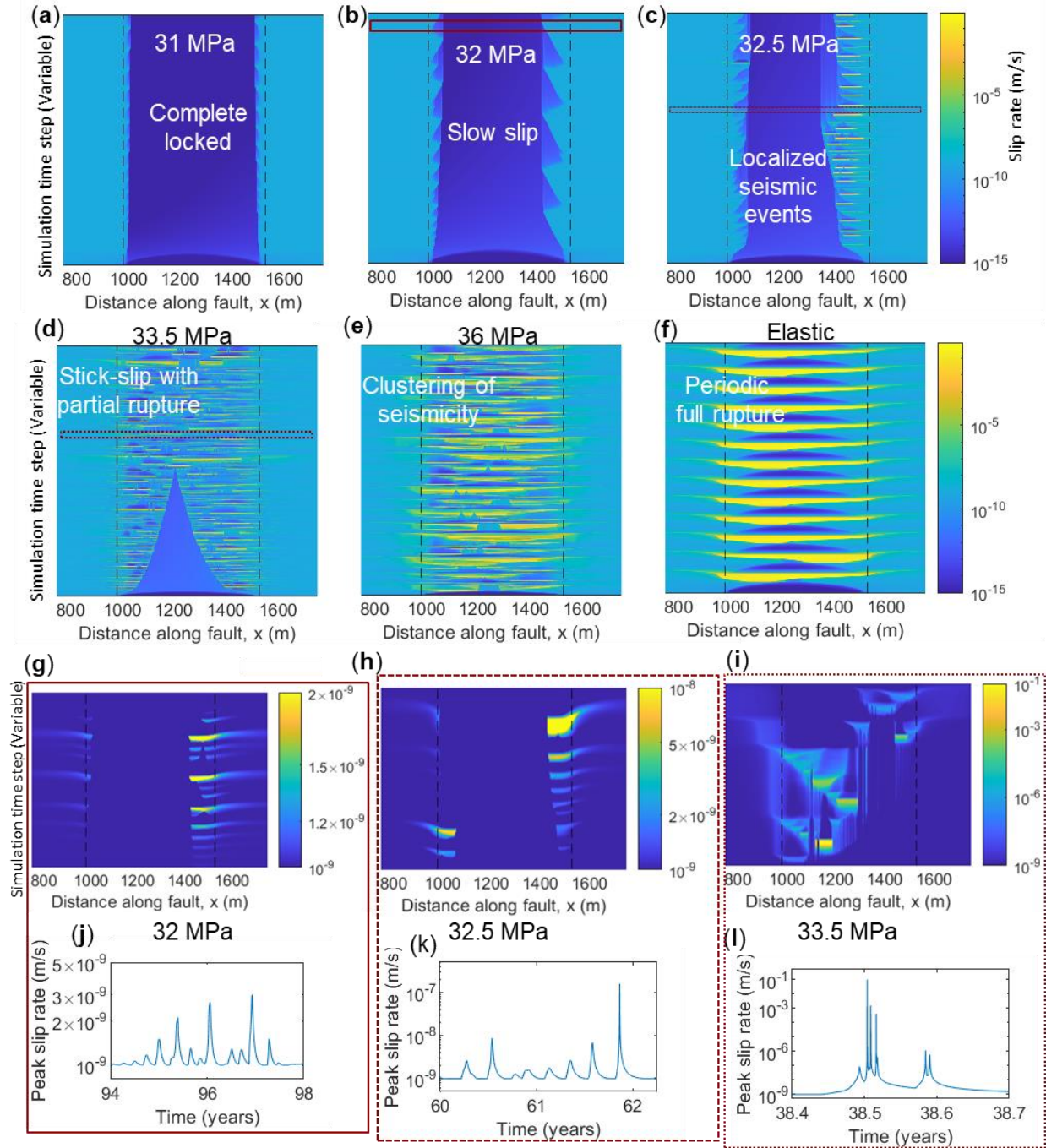
174 Spatially, these events are localized near the transition region from VS to VW. Similar spatially
175 localized slow slip events are also observed in between localized partial ruptures for yield strength
176 32.5 MPa (Figure-2c, 2h, 2k). However, the peak slip rate associated with some of these aseismic
177 transients reaches orders of magnitude higher than the background plate rate. The irregular pattern
178 with yield strength 33.5 MPa also includes slow slip events (Figure-2d, 2i, 2l). The peak slip rates
179 associated with these slow slip events are even higher, but they are still below the seismic
180 threshold. These slow slip events, observed with yield strength 33.5 MPa, are no longer localized
181 in the transition region. Rather they show spatial migration over the full length of the seismogenic
182 (Velocity-Weakening) patch of the fault.

183 **Localized seismic events:** A repeating pattern of localized seismic events is observed for yield
184 strength 32.5 MPa as shown in Figure-2c. These seismic events are inter-mixed with slow slip
185 episodes as described above. The seismic events are spatially localized near the boundary between
186 VS and VW. They rupture approximately the same area, but they do not repeat with the exact
187 return period (Supplementary Figure-S2c). Their average stress drop is around 2.3 MPa with
188 standard deviation of 0.5 MPa approximately which is consistent with stress drop measured for
189 earthquake repeaters (Chen & Lapusta, 2009). The slow slip events observed in this case occur
190 mostly before the seismic events.

191 **Stick-slip with partial ruptures:** When yield strength is increased to 33.5 MPa, fault sliding
192 includes slow slip and partial seismic ruptures (Figure-2d). In the early stages of the sequence,
193 partial ruptures extend on both sides of fault, but a locked patch remains in the center that gets
194 progressively narrower with time. Later in the cycle, the whole VW region is ruptured by
195 subsequent partial events. Here the partial ruptures are prevalent throughout the VW patch unlike

196 the localized repeating events shown in Figure-2b. Also, the clustering of events observed with
197 relatively higher yield strength e.g., 36 MPa (Figure-2e) is not found for the case with yield
198 strength 33.5 MPa.

199 **Stick-slip with fault-spanning ruptures:** For relatively higher yield strength (e.g., 36 MPa
200 shown in Figure-2e), seismic events, including partial ruptures as well as ruptures spanning the
201 full VW patch, dominate the slip pattern. Evolution of the spatial extent of rupture, discussed above
202 for lower yield strength, showing central locked patches progressively unclamped with time does
203 not exist with relatively higher yield strength. The resulting sequence, including partial and fault-
204 spanning rupture, is aperiodic with clustering of seismic events in space and time. Simulation with
205 elastic bulk (Figure-2f) results in simple periodic cycle with fault-spanning ruptures only. Cycle
206 simulations for a range of high values of yield strength and post-yield viscosity are discussed in
207 our previous study (Mia et al., 2022) where seismicity pattern changes from complex spatio-
208 temporal clustering to simple periodic pattern with increasing yield strength and post-yield
209 viscosity. While here we adopted a quasi-dynamic approximation of inertia effect through a
210 radiation damping term, the results are qualitatively similar even if we consider full inertia effects
211 (Supplementary Information, Figure-S2).



213
 214 **Figure 2.** Spectrum of slip for a rate-and-state fault. Spatio-temporal evolution of slip rate illustrating different slip
 215 pattern for different yield strength (a-e). Elastic case results in periodic seismic cycle as shown in f. Region between
 216 two vertical dashed lines correspond to velocity weakening friction. Fault reference strength is $\sigma_n f_o = 30$ MPa. Fault
 217 remains locked for yield strength, $\sigma_y = 31$ MPa. Locked fault with occasional slow slip is found for $\sigma_y = 32$ MPa .
 218 Localized earthquakes near the transition between VS and VW are shown in c. Complex pattern including slow slip
 219 and seismic events with partial rupture is shown in d. Clustering of seismicity is found when yield strength is increased
 220 (e). Closer examination of example of slow slip events that exist with $\sigma_y = 32, 32.5$ and 33.5 MPa are shown in g-l.

221 **Partitioning of deformation**

222 Plasticity results in a slip deficit on the fault surface through partitioning of total deformation into
223 on-fault slip and off-fault plastic deformation. In Figure-3, the spatial distribution of the
224 cumulative slip and off-fault plastic deformation is shown for yield strength 33.5 MPa. Here we
225 calculate an effective measure for the variation of the plastic deformation in the fault zone along
226 the fault length by integrating the equivalent plastic strain, γ , as $u_p(x, t) = 2 \int_0^{L_y} \gamma(x, y, t) dy$,
227 where, L_y is the half width of the computational strip modeled using FEM, and y represents the
228 spatial direction normal to the fault plane. The factor of 2 accounts for the symmetry of the plastic
229 strain distribution about the fault surface. This is characteristics of anti-plane plasticity in
230 homogeneous media where the normal stress does not change with deformation. For the current
231 model geometry, $L_y = 30$ m which is around 1.5 times the process zone size. This width is found
232 sufficient to contain the spatial extent of plasticity in the fault normal direction. Outside this
233 computational strip, the exterior half-spaces are elastic and are modeled using the spectral
234 boundary integral approach. Therefore, they do not experience plastic deformation. Total plastic
235 deformation along the fault, $u_p(x, t)$ is shown in Figure-3b. Cumulative slip is plotted in Figure-
236 3a. The contour lines for both quantities are plotted every 10 years up to 50 years.

237 As shown in Figure-3a, cumulative slip in the VS patch is around 1.5 m in 50 years. Slip
238 accumulation is reduced near the transition from VS to VW and is further reduced in the interior
239 of the locked VW region. The central region of the VW patch is locked in early stages. As time
240 passes, seismic events progressively unlock the VW fault through a sequence of partial ruptures
241 as shown in Figure-2d. The non-smooth shape of the cumulative slip lines corresponds to the
242 irregular pattern of slow slip and partial ruptures spreading over the whole VW region. From the

243 plastic deformation plot (Figure-3b), it is evident that plastic deformation in the bulk compensates
244 for the slip deficit in the VW patch. Plastic deformation is maximum in the central part of the VW
245 patch where the fault slip is minimum and gradually vanishes towards the VS region.

246 Off-fault plastic deformation gets an increasing share of the total deformation budget when the
247 bulk yield strength is lower. To evaluate the partitioning of deformation and associated slip pattern
248 for different values of yield strength, we compute the on-fault deformation by integrating fault slip
249 termed as Potency (t) = $\int_0^{L_f} d(x, t)dx$, and off-fault plastic deformation by integrating the
250 equivalent plastic strain over the domain as $PD(t) = \int_S \gamma(x, y, t)dS$. Where d is the slip, L_f is
251 the seismogenic region of the fault including VW patch and the transition region between VW and
252 VS, and S is the area of the 2D elastoplastic fault zone. For all the cases shown in Figure-3c, there
253 is an initial increase of plastic deformation while the potency is small. This indicates plasticity
254 accumulation when the fault is locked prior to any seismic events. When fault slip occurs, both
255 potency and plastic deformation increases but the increment of plastic deformation is relatively
256 lower. For the cases shown in Figure-3c, the ratio between plastic deformation and potency varies
257 over an order of magnitude ranging from ~ 0.1 for $\sigma_y = 36$ MPa to ~ 3.5 for $\sigma_y = 32$ MPa.

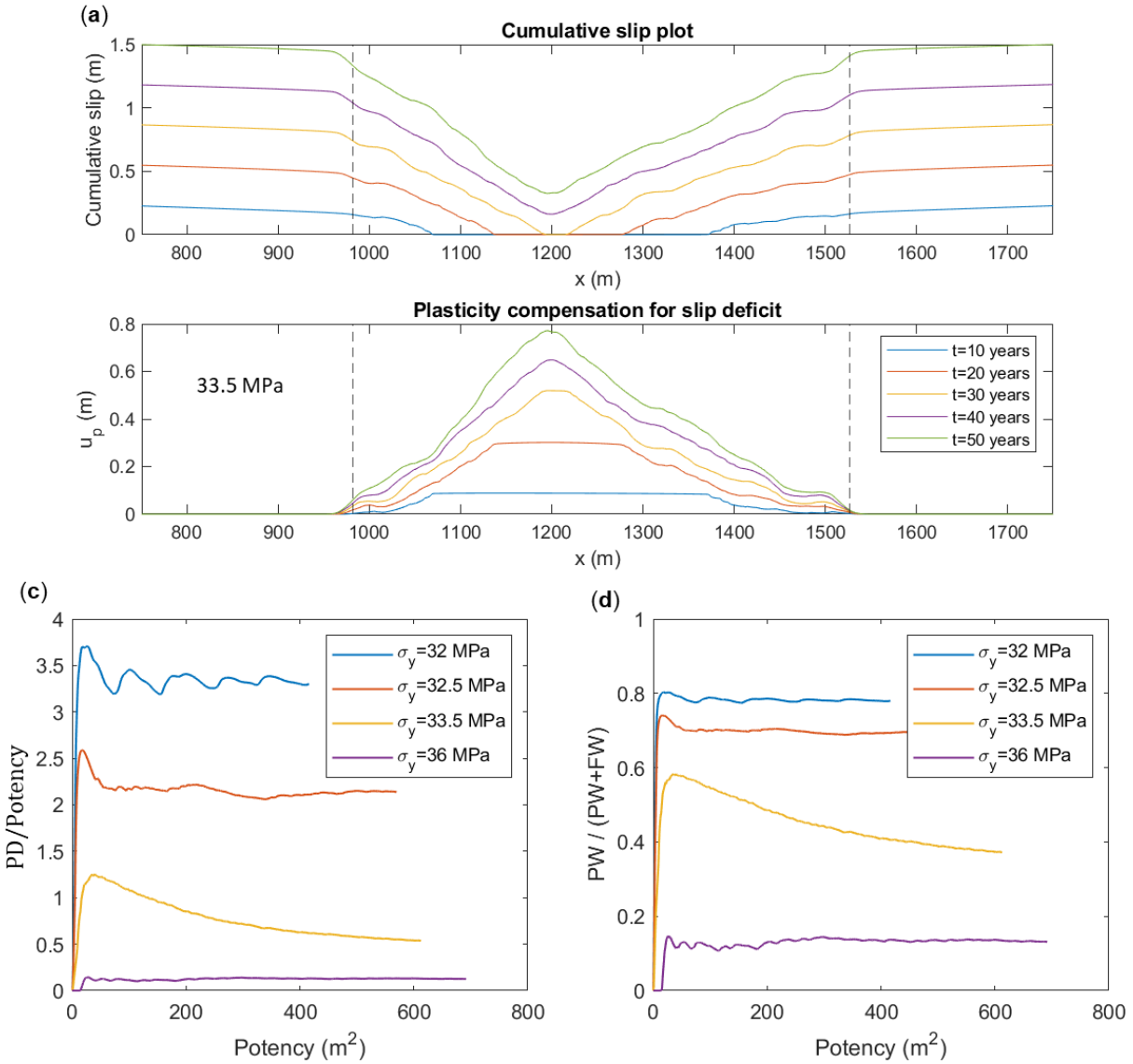
258 For the same amount of potency, plastic deformation is higher with lower yield strength. The
259 pattern of slip with clustered seismic events ($\sigma_y = 36$ MPa , shown in Figure-2,3) is associated
260 with relatively lower plastic deformation to potency ratio (~ 0.1). However, fault slip involving
261 slow slip and partial ruptures spreading over the fault ($\sigma_y = 33.5$ MPa , shown in Figure-2,3)
262 correspond to higher ratios of plastic deformation to potency (~ 0.5). Localized seismic event and
263 slow slip in otherwise locked fault ($\sigma_y = 32.5$ MPa, $\sigma_y = 32$ MPa shown in Figure-2,3)

264 corresponds to relatively higher plastic deformation to potency ratio (> 1). In these limits of low
265 yield strength, more deformation is distributed in the bulk than localized as slip on the fault surface.

266 Figure-3d shows the ratio of plastic dissipation relative to total dissipation. Total dissipation is the
267 sum of plastic dissipation (PW) and frictional dissipation (FW). Here, frictional dissipation is
268 computed over the region of the fault used to compute the potency. This region includes the VW
269 patch as well as the transition regions between the VW and VS patches. That is, we do not account
270 for frictional dissipation due to slip in the VS region which conforms to the plate loading.

271 Contribution of plastic dissipation is higher with lower yield strength. On one hand, for the case
272 of $\sigma_y = 32$ MPa , generating slow slip events, plastic dissipation is around 80% of the total
273 dissipation. On the other hand, clustered seismic events with $\sigma_y = 36$ MPa is associated with much
274 lower plastic dissipation ($\sim 10\%$ of total dissipation). The decrease in the ratio of plastic to total
275 dissipation is a result of less off-fault plastic deformation and corresponds to higher frictional
276 dissipation through fault slip in large and fast seismic events. Higher off-fault deformation and
277 smaller on-fault slip leads to increased off-fault dissipation. Mia et al., 2022, showed that even if
278 the contribution of plasticity to the energy budget is small, it may still play a significant role in
279 regulating the spatio-temporal clustering of seismic events through limiting the stress
280 concentration ahead of the rupture tip and facilitating rupture arrest. Here, we additionally show
281 that if the energy dissipation is dominated by off-fault plastic dissipation, which happens for lower
282 yield strength, fault-spanning events cannot occur and slip becomes progressively slower.

283 Specifically, we observe that irregular partial ruptures, slow slip, repeaters, and even complete
284 locking of the VW patch emerge in the limit of low yield strength and increased off-fault plastic
285 dissipation irrespective of fault length. This further suggests that plastic dissipation should be low
286 (less than 10%) compared to total dissipation, in order for large fault spanning events to occur.



287
 288 **Figure 3.** Plasticity compensation for slip deficit and partitioning of deformation as well as energy dissipation between
 289 the bulk and the fault. (a) Cumulative slip is plotted at an interval of 10 years (for $\sigma_y = 33.5$ MPa). (b) Off-fault
 290 plastic deformation obtained from integrating the plastic strain in lateral direction is plotted along the fault in the same
 291 interval of cumulative slip plot (for $\sigma_y = 33.5$ MPa). The region within the two vertical dashed lines corresponds to
 292 the fault section with velocity weakening friction. The extent of locked region subsequently shrinks with increased
 293 slip. Plasticity compensation is higher in the region where slip accumulation is lower. (c) Relative contribution of on-
 294 fault slip and off-fault plastic deformation. Potency is computed by integrating slip, $Potency(t) = \int_0^{L_f} d(x, t) dx$ and
 295 plastic deformation is computed from integrating the plastic strain over the domain, $PD(t) = \int_S \gamma(x, y, t) dS$. Lower
 296 yield strength corresponds to higher amount of plastic deformation. (d) Plot of plastic energy dissipation (PW)
 297 relative to total dissipation. FW is the frictional dissipation computed over the velocity weakening patch and the transition
 298 region. Higher percentage of plastic dissipation is associated with lower yield strength generating slow slip.

299 **4. Discussion**

300 In this work, we showed, using a simple elastoplastic spring block model, that spring stiffness,
301 even when lower than the critical value for instability predicted by elastic analysis, may not
302 facilitate stick-slip instability if the yield strength is low enough. Since stiffness is inversely
303 proportional to length, this finding suggests that not all perturbations with wavelength greater than
304 the nucleation length are unstable. Rather the maximum wavelength that is unstable may vary
305 depending on yield strength. This implies that there may exist a maximum rupture length, when
306 off-fault plasticity is considered, irrespective of how large the fault is. Similar patterns are
307 observed in continuum 2D anti-plane simulations with different values of yield strength. The rich
308 slip patterns observed in the continuum model include locked fault, slow slip events, localized
309 sequence of seismic event and irregular patterns with partial ruptures spreading over the fault.
310 Neither frictional heterogeneity nor pore pressure perturbation is introduced here. Only the bulk
311 strength is acting as the controlling factor in modulating the slip pattern.

312 In a characteristic seismic cycle, VS patch accumulates slip during the interseismic period and VW
313 patch catches up with seismic slip accumulation. However, when the bulk strength is relatively
314 low, seismic events are rare or spatially limited with partial ruptures. This results in slip deficit
315 prevailing throughout the seismic cycle. We found that off-fault plastic deformation compensates
316 for the slip deficit in this case. For sufficiently low bulk strength, fault may remain locked without
317 generating seismic events while off-fault bulk accommodates the deformation through plastic
318 deformation. This is also analogous to the spring slider results where plastic deformation in the
319 spring resists and even, in some cases, prevents the sliding of the block. Relative amount of off-
320 fault plastic deformation and on-fault slip is associated with the spectrum of slip from clustered

321 fast slip to a mixture of fast and slow slip as the yield strength decreases. Inelastic dissipation must
322 remain low for fast fault large events to exist.

323 We note that large amount of shallow off-fault deformation, exceeding 80% of the total surface
324 deformation (i.e., 4 times the on-fault slip) has been reported around some faults recently by Li et
325 al., (2022). They hypothesized that the large amount of off-fault deformation may include some
326 elastic deformation. The determination of the extent of inelastic off-fault deformation would be
327 possible if additional data from seismic reflection was available. The plastic strain in our simulation
328 is limited to a narrow region close to the fault (Supplementary Figure-S4). If this holds true for
329 off-fault plasticity accumulation in natural fault zones, particularly at depth, it may be difficult to
330 distinguish between on-fault and off-fault deformation from field observations specially from
331 satellite measurements as there are limitations on high resolution measurements of off-fault
332 deformation (Antoine et al., 2021). This partitioning of deformation is, however, important to
333 quantify as accumulation of off-fault plasticity may have implications for fault weakening. As
334 plastic deformation involves dissipation over narrow but finite region, it can influence the heat
335 diffusion and constrain the rise of temperature associated with slip localization into an extremely
336 thin surface in an otherwise elastic medium (Rice 2006). This may contribute to understanding the
337 scarcity of fault zone melting in some field observations. However, since most of the plastic
338 dissipation is still in the form of heat, we do not think that off-fault plasticity resolves the heat flow
339 anomaly.

340 Slow slip events recorded in some field observations show a wide range of durations in the scale
341 of days to months, and large earthquakes have been found after the migration of slow slip events
342 and small earthquakes (Ito et al., 2013; Ruiz et. al., 2014; Obara & Kato, 2016). The coexistence
343 of slow slip events and small earthquakes in subduction zone has also been reported by Ito et al.,

344 2007. In our simulation, fault slip accompanied by a mixture of seismic events with partial ruptures
345 and slow slip events are observed. Some of the slow slip events show spatial migration over the
346 seismogenic patch with duration reaching the scale of months. We observe emergence of spectrum
347 of slip by simulating different cases with small difference in yield strength. In natural fault zone,
348 off-fault bulk property (for example, yield strength) may vary spatially and evolve with time. Since
349 yield strength depends on effective normal stress, physical process like fluid pressure perturbation
350 may alter the yield strength independent of fault strength alteration depending on the hydraulic
351 properties in the fault core relative to the fault zone. Healing of damaged fault zone may also
352 contribute to the evolution of yield strength. Consequently, a fault may host different patterns of
353 slip switching from fast seismic rupture to slow aseismic slip when yield strength transiently
354 decreases.

355 The localized seismic events observed in our continuum simulations, at the boundary of the VW
356 and VS regions, is analogous to repeating microseismicity model presented in Sammis & Rice
357 (2000) but some differences exist. The similarity is that the location of the seismic events is near
358 the transition between creeping asperity (VS patch) and seismogenic locked asperity (VW patch).
359 The slip deficit in their model is compensated by occasional full-fault spanning events whereas the
360 slip deficit in our simulations is compensated by off-fault plastic deformation. Also, in our
361 simulations, there are slow slip events in between the seismic events.

362 In this model, we consider the frictional parameters like reference friction coefficient, direct effect,
363 and state evolution coefficient to remain stationary. However, frictional parameters may evolve
364 with coseismic deformation (Kaproth & Marone, 2013; Im et al., 2020) which may get pronounced
365 with off-fault damage or plasticity accumulation. Investigating the interplay between evolving
366 fault friction as well as degradation and subsequent healing of fault zone material warrants future

367 study. Fault zone geometric complexity including nonplanar fault, and interaction of multiple
368 faults in presence of off-fault material non-linearity is planned as future study. Furthermore,
369 evolution of pore pressure associated with volumetric deformation of the fault zone need to be
370 considered for its vast implications on the evolution of strength and deformation in fluid-saturated
371 fault zones.

372 **Acknowledgement**

373 The authors acknowledge support from the Southern California Earthquake Center through a
374 collaborative agreement between NSF. Grant Number: EAR0529922 and USGS. Grant Number:
375 07HQAG0008 and the National Science Foundation CAREER award No. 1753249 for modeling
376 complex fault zone structures. This material is also based upon work partially supported by the
377 Department of Energy under Award Number DE-FE0031685 to investigate spatio-temporal
378 complexity of induced earthquakes.

379 **Data Availability Statement**

380 The authors accept the data policy. Data generated from the numerical simulations are uploaded
381 on an open access repository (10.5281/zenodo.7718768).

382 **References**

- 383 Abdelmeguid, M., Ma, X., & Elbanna, A. (2019). A Novel Hybrid Finite Element-Spectral Boundary
384 Integral Scheme for Modeling Earthquake Cycles: Application to Rate and State Faults With Low-
385 Velocity Zones. *Journal of Geophysical Research: Solid Earth*, 124(12), 12854–12881.
386 <https://doi.org/10.1029/2019JB018036>
- 387 Abdelmeguid, M., & Elbanna, A. (2022a). Sequences of seismic and aseismic slip on bimaterial faults show
388 dominant rupture asymmetry and potential for elevated seismic hazard. *Earth and Planetary Science*
389 *Letters*, 593. <https://doi.org/10.1016/j.epsl.2022.117648>
- 390 Abdelmeguid, M., & Elbanna, A. (2022b). Modeling Sequences of Earthquakes and Aseismic Slip (SEAS)
391 in Elasto-Plastic Fault Zones With a Hybrid Finite Element Spectral Boundary Integral Scheme.
392 *Journal of Geophysical Research: Solid Earth*, 127(12). <https://doi.org/10.1029/2022JB024548>

393 Allison, K. L., & Dunham, E. M. (2021). Influence of Shear Heating and Thermomechanical Coupling on
394 Earthquake Sequences and the Brittle-Ductile Transition. *Journal of Geophysical Research: Solid*
395 *Earth*, 126(6). <https://doi.org/10.1029/2020JB021394>

396 Ampuero, J. P., & Rubin, A. M. (2008). Earthquake nucleation on rate and state faults - Aging and slip
397 laws. *Journal of Geophysical Research: Solid Earth*, 113(1). <https://doi.org/10.1029/2007JB005082>

398 Antoine, S. L., Klinger, Y., Delorme, A., Wang, K., Bürgmann, R., & Gold, R. D. (2021). Diffuse
399 deformation and surface faulting distribution from submetric image correlation along the 2019
400 Ridgecrest, California, ruptures. *Bulletin of the Seismological Society of America*, 111(5), 2275-2302.
401 <https://doi.org/10.1785/0120210036>

402 Avouac, J. P. (2015). From geodetic imaging of seismic and aseismic fault slip to dynamic modeling of the
403 seismic cycle. *Annual Review of Earth and Planetary Sciences*, 43, 233–271.
404 <https://doi.org/10.1146/annurev-earth-060614-105302>

405 Barbot, S., Lapusta, N., & Avouac, J.-P. (2012). Under the Hood of the Earthquake Machine: Toward
406 Predictive Modeling of the Seismic Cycle. *Science*, 336(6082), 707–710.
407 <https://doi.org/10.1126/science.1218796>

408 Barbot, S. (2019). Slow-slip, slow earthquakes, period-two cycles, full and partial ruptures, and
409 deterministic chaos in a single asperity fault. *Tectonophysics*, 768.
410 <https://doi.org/10.1016/j.tecto.2019.228171>

411 Bedford, J. D., Faulkner, D. R., & Lapusta, N. (2022). Fault rock heterogeneity can produce fault weakness
412 and reduce fault stability. *Nature Communications*, 13(1). <https://doi.org/10.1038/s41467-022-27998-2>

413 Ben-Zion, Y., & Rice, J. R. (1993). Earthquake failure sequences along a cellular fault zone in a three-
414 dimensional elastic solid containing asperity and nonasperity regions. *Journal of Geophysical*
415 *Research*, 98(B8). <https://doi.org/10.1029/93jb01096>

416 Ben-Zion, Y., & Sammis, C. G. (2003). Characterization of Fault Zones. In *Pure appl. geophys* (Vol. 160).
417 Birkhäuser Verlag.

418 Beroza, G. C., & Ide, S. (2011). Slow earthquakes and nonvolcanic tremor. *Annual Review of Earth and*
419 *Planetary Sciences*, 39, 271–296. <https://doi.org/10.1146/annurev-earth-040809-152531>

420 Bürgmann, R. (2018). The geophysics, geology and mechanics of slow fault slip. *Earth and Planetary*
421 *Science Letters*, 495, 112–134. <https://doi.org/10.1016/j.epsl.2018.04.062>

422 Cattania, C. (2019). Complex Earthquake Sequences On Simple Faults. *Geophysical Research Letters*,
423 46(17–18), 10384–10393. <https://doi.org/10.1029/2019GL083628>

424 Chen, T., & Lapusta, N. (2009). Scaling of small repeating earthquakes explained by interaction of seismic
425 and aseismic slip in a rate and state fault model. *J. Geophys. Res.*, 114, 1311.
426 <https://doi.org/10.1029/2008JB005749>

427 Chen, Y., Liu, M., & Luo, G. (2020). Complex temporal patterns of large earthquakes: Devil’s staircases.
428 *Bulletin of the Seismological Society of America*, 110(3), 1064–1076.
429 <https://doi.org/10.1785/0120190148>

430 Collettini, C., Barchi, M. R., de Paola, N., Trippetta, F., & Tinti, E. (2022). Rock and fault rheology explain
431 differences between on fault and distributed seismicity. *Nature Communications*, 13(1).
432 <https://doi.org/10.1038/s41467-022-33373-y>

- 433 Dragert, H., Wang, K., & James, T. S. (2001). A Silent Slip Event on the Deeper Cascadia Subduction
434 Interface. *Science*, 292(5521), 1525–1528. <https://doi.org/10.1126/science.1060152>
- 435 Erickson, B. A., Jiang, J., Lambert, V., Barbot, S. D., Abdelmeguid, M., Almquist, M., Ampuero, J.-P.,
436 Ando, R., Cattania, C., Chen, A., Dal Zilio, L., Deng, S., Dunham, E. M., Elbanna, A. E., Gabriel, A.-
437 A., Harvey, T. W., Huang, Y., Kaneko, Y., Kozdon, J. E., ... Yang, Y. (2023). Incorporating Full
438 Elastodynamic Effects and Dipping Fault Geometries in Community Code Verification Exercises for
439 Simulations of Earthquake Sequences and Aseismic Slip (SEAS). *Bulletin of the Seismological Society
440 of America*. <https://doi.org/10.1785/0120220066>
- 441 French, M. E., & Zhu, W. (2017). Slow fault propagation in serpentinite under conditions of high pore fluid
442 pressure. *Earth and Planetary Science Letters*, 473, 131-140.
443 <https://doi.org/10.1016/j.epsl.2017.06.009>
- 444 Goswami, A., & Barbot, S. (2018). Slow-slip events in semi-brittle serpentinite fault zones. *Scientific
445 Reports*, 8(1). <https://doi.org/10.1038/s41598-018-24637-z>
- 446 Heki, K., & Kataoka, T. (2008). On the biannually repeating slow-slip events at the Ryukyu Trench,
447 southwestern Japan. *Journal of Geophysical Research: Solid Earth*, 113(11).
448 <https://doi.org/10.1029/2008JB005739>
- 449 Im, K., Saffer, D., Marone, C., & Avouac, J. P. (2020). Slip-rate-dependent friction as a universal
450 mechanism for slow slip events. *Nature Geoscience*, 13(10), 705–710. [https://doi.org/10.1038/s41561-
451 020-0627-9](https://doi.org/10.1038/s41561-020-0627-9)
- 452 Ito, Y., Hino, R., Kido, M., Fujimoto, H., Osada, Y., Inazu, D., Ohta, Y., Iinuma, T., Ohzono, M., Miura,
453 S., Mishina, M., Suzuki, K., Tsuji, T., & Ashi, J. (2013). Episodic slow slip events in the Japan
454 subduction zone before the 2011 Tohoku-Oki earthquake. *Tectonophysics*, 600, 14–26.
455 <https://doi.org/10.1016/j.tecto.2012.08.022>
- 456 Ito, Y., Obara, K., Shiomi, K., Sekine, S., & Hirose, H. (2007). Slow earthquakes coincident with episodic
457 tremors and slow slip events. *Science*, 315(5811), 503-506. <https://doi.org/10.1126/science.1134454>
- 458 Jiang, J., Erickson, B. A., Lambert, V. R., Ampuero, J. P., Ando, R., Barbot, S. D., Cattania, C., Zilio, L.
459 D., Duan, B., Dunham, E. M., Gabriel, A. A., Lapusta, N., Li, D., Li, M., Liu, D., Liu, Y., Ozawa, S.,
460 Pranger, C., & van Dinther, Y. (2022). Community-Driven Code Comparisons for Three-Dimensional
461 Dynamic Modeling of Sequences of Earthquakes and Aseismic Slip. *Journal of Geophysical Research:
462 Solid Earth*, 127(3). <https://doi.org/10.1029/2021JB023519>
- 463 Kaproth, B. M., & Marone, C. (2013). Slow Earthquakes, Preseismic Velocity Changes, and the Origin of
464 Slow Frictional Stick-Slip. *Science*, 341(6151), 1229–1232. <https://doi.org/10.1126/science.1239577>
- 465 Kaneko, Y., Avouac, J. P., & Lapusta, N. (2010). Towards inferring earthquake patterns from geodetic
466 observations of interseismic coupling. *Nature Geoscience*, 3(5), 363–369.
467 <https://doi.org/10.1038/ngeo843>
- 468 Lapusta, N., Rice, J. R., Ben-Zion, Y., & Zheng, G. (2000). Elastodynamic analysis for slow tectonic
469 loading with spontaneous rupture episodes on faults with rate- and state-dependent friction. *Journal of
470 Geophysical Research: Solid Earth*, 105(B10), 23765–23789. <https://doi.org/10.1029/2000jb900250>
- 471 Lewis, M. A., & Ben-Zion, Y. (2010). Diversity of fault zone damage and trapping structures in the
472 Parkfield section of the San Andreas Fault from comprehensive analysis of near fault seismograms.
473 *Geophysical Journal International*, 183(3), 1579–1595. [https://doi.org/10.1111/j.1365-
474 246X.2010.04816.x](https://doi.org/10.1111/j.1365-246X.2010.04816.x)

- 475 Li, C., Li, T., Shan, X., & Zhang, G. (2022). Extremely Large Off-Fault Deformation during the 2021
476 Mw 7.4 Maduo, Tibetan Plateau, Earthquake. *Seismological Research Letters*.
477 <https://doi.org/10.1785/0220220139>
- 478 Liu, Y., & Rice, J. R. (2007). Spontaneous and triggered aseismic deformation transients in a subduction
479 fault model. *Journal of Geophysical Research: Solid Earth*, 112(9).
480 <https://doi.org/10.1029/2007JB004930>
- 481 Mia, M. S., Abdelmeguid, M., & Elbanna, A. E. (2022). Spatio-Temporal Clustering of Seismicity Enabled
482 by Off-Fault Plasticity. *Geophysical Research Letters*, 49(8). <https://doi.org/10.1029/2021GL097601>
- 483 Mitchell, T. M., & Faulkner, D. R. (2009). The nature and origin of off-fault damage surrounding strike-
484 slip fault zones with a wide range of displacements: A field study from the Atacama fault system,
485 northern Chile. *Journal of Structural Geology*, 31(8), 802–816.
486 <https://doi.org/10.1016/j.jsg.2009.05.002>
- 487 Miyake, Y., & Noda, H. (2019). Fully dynamic earthquake sequence simulation of a fault in a viscoelastic
488 medium using a spectral boundary integral equation method: does interseismic stress relaxation
489 promote aseismic transients?. *Earth, Planets and Space*, 71(1), 1-12.
- 490 Nie, S., & Barbot, S. (2022). Rupture styles linked to recurrence patterns in seismic cycles with a compliant
491 fault zone. *Earth and Planetary Science Letters*, 591. <https://doi.org/10.1016/j.epsl.2022.117593>
- 492 Nakata, R., Ando, R., Hori, T., & Ide, S. (2011). Generation mechanism of slow earthquakes: Numerical
493 analysis based on a dynamic model with brittle-ductile mixed fault heterogeneity. *Journal of*
494 *Geophysical Research: Solid Earth*, 116(8). <https://doi.org/10.1029/2010JB008188>
- 495 Noda, H., & Lapusta, N. (2013). Stable creeping fault segments can become destructive as a result of
496 dynamic weakening. *Nature*, 493(7433), 518–521. <https://doi.org/10.1038/nature11703>
- 497 Obara, K., & Kato, A. (2016). Connecting slow earthquakes to huge earthquakes. *Science*, 353(6296), 253-
498 257. <https://doi.org/10.1126/science.aaf1512>
- 499 Radiguet, M., Cotton, F., Vergnolle, M., Campillo, M., Walpersdorf, A., Cotte, N., & Kostoglodov, V.
500 (2012). Slow slip events and strain accumulation in the Guerrero gap, Mexico. *Journal of Geophysical*
501 *Research: Solid Earth*, 117(4). <https://doi.org/10.1029/2011JB008801>
- 502 Ranjith, K., & Rice, J. R. (1999). Stability of quasi-static slip in a single degree of freedom elastic system
503 with rate and state dependent friction. *Journal of the Mechanics and Physics of Solids*, 47(6), 1207-
504 1218. [https://doi.org/10.1016/S0022-5096\(98\)00113-6](https://doi.org/10.1016/S0022-5096(98)00113-6)
- 505 Rice, J. R. (2006). Heating and weakening of faults during earthquake slip. *Journal of Geophysical*
506 *Research: Solid Earth*, 111(5). <https://doi.org/10.1029/2005JB004006>
- 507 Rice, J. R., & Ruina, A. L. (1983). Stability of Steady Frictional Slipping. In *Journal of Applied*
508 *Mechanics*, 50(2), 343-349. <https://doi.org/10.1115/1.3167042>
- 509 Rice, J. R., Lapusta, N., & Ranjith, K. (2001). Rate and state dependent friction and the stability of sliding
510 between elastically deformable solids. *Journal of the Mechanics and Physics of Solids*, 49(9), 1865-
511 1898. [https://doi.org/10.1016/S0022-5096\(01\)00042-4](https://doi.org/10.1016/S0022-5096(01)00042-4)
- 512 Ross, Z. E., Cochran, E. S., Trugman, D. T., &
513 Smith, J. D. (2020). 3D fault architecture controls the dynamism of earthquake swarms. *Science*,
368(6497), 1357–1361. <https://doi.org/10.1126/science.abb0779>
- 514 Ruiz, S., Metois, M., Fuenzalida, A., Ruiz, J., Leyton, F., Grandin, R., ... & Campos, J. (2014). Intense
515 foreshocks and a slow slip event preceded the 2014 Iquique M w 8.1 earthquake. *Science*, 345(6201),
516 1165-1169. <https://doi.org/10.1126/science.1256074>

- 517 Sammis, C. G., & Rice, J. R. (2000). *Repeating Earthquakes as Low-Stress-Drop Events at a Border*
518 *between Locked and Creeping Fault Patches.*
- 519 Segall, P., Rubin, A. M., Bradley, A. M., & Rice, J. R. (2010). Dilatant strengthening as a mechanism for
520 slow slip events. *Journal of Geophysical Research: Solid Earth*, 115(12).
521 <https://doi.org/10.1029/2010JB007449>
- 522 Skarbek, R. M., Rempel, A. W., & Schmidt, D. A. (2012). Geologic heterogeneity can produce aseismic
523 slip transients. *Geophysical Research Letters*, 39(21). <https://doi.org/10.1029/2012GL053762>
- 524 Wu, B. (2021). *Explaining Slow Earthquake Phenomena with a Frictional-Viscous Faulting*
525 *Model* (Doctoral dissertation, University of California, Riverside).

Supplementary Information for

The Spectrum of Fault Slip in Elastoplastic Fault Zones

Md Shumon Mia^{1,2}, Mohamed Abdelmeguid^{2,3}, Ahmed E. Elbanna^{2,4}

¹Department of Mechanical Science and Engineering, University of Illinois at Urbana-Champaign, Urbana, IL, USA.

²Department of Civil and Environmental Engineering, University of Illinois at Urbana-Champaign, Urbana, IL, USA.

³Graduate Aerospace Laboratories, California Institute of Technology, Pasadena, CA, USA.

⁴Beckman Institute of Advanced Science and Technology, University of Illinois at Urbana-Champaign, Urbana, IL, USA.

Corresponding author: Md Shumon Mia (mmia2@illinois.edu)

Contents of this file

Text S1 to S2
Tables S1
Figures S1 to S4

Introduction

The Supplementary Information includes:

- Text S1 outlines the model setup and methods.
- Table S1 provides input parameters for the simulations.
- Figure S1 shows model geometry and hybrid scheme setup.
- Figure S2 shows history of peak slip rate for simulations with different yield strength and elastic case .
- Figure S3 shows results of fully dynamics simulations for yield strength 33.5 MPa, 36 MPa and elastic case. Slip patterns are qualitatively similar to the quasi-dynamics cases presented in the main text.
- Figure S4 shows spatial extent of off-fault plasticity for yield strength 33.5 MPa.

Text S1. Rate-and-state friction

The fault friction is governed by a regularized rate-and-state friction law (Dieterich, 1979; Ruina, 1983; Ben-Zion & Rice, 1997; Lapusta et al., 2000) where the friction coefficient, f , is a function of slip rate, V , and state variable, θ .

$$f(V, \theta) = a \sinh^{-1} \left[\frac{V}{2V_0} \exp \left(\frac{f_0 + b \ln(V_0 \theta / L)}{a} \right) \right] \quad (\text{Eqn-1}).$$

Here, a and b are non-negative dimensionless frictional parameters related to direct effect and state evolution respectively. $a < b$ indicates velocity weakening friction whereas $a > b$ indicates velocity strengthening friction. f_0 is the reference friction coefficient with a reference slip rate V_0 . L is critical slip weakening distance. State variable, θ , refers to the time of contact between the sliding asperities which evolves following a prescribed aging law (Ruina, 1983; Ampuero & Rubin, 2008):

$$\frac{d\theta}{dt} = 1 - \frac{V\theta}{L} \quad (\text{Eqn-2}).$$

For constant normal stress, σ_n , fault strength is then expressed as $\sigma_n f(V, \theta)$. In case of pore pressure perturbation $P(x, t)$, effective normal stress is $\sigma_e(x, t) = \sigma_n - P(x, t)$, and fault strength becomes $\sigma_e(x, t) f(V, \theta)$. We model dry case considering no perturbation of pore pressure i.e., $\sigma_e(x, t) = \sigma_n$. Approximating inertia with radiation damping, called quasi-dynamics approach (Rice 1993; Ranjith & Rice, 1999), shear stress in the frictional interface is given by,

$$\tau = \sigma_e f(V, \theta) + \eta_r V \quad (\text{Eqn-3}).$$

Where the radiation damping coefficient is given by $\eta_r = \frac{\mu}{2c_s}$.

Text S2. Model Setup and Methods

The model includes frictional interface (fault) embedded in a 2D whole space (Figure-S1).

Balance of linear momentum leads to the equilibrium equation:

$$\sigma_{ij,j} + b_i = \rho \ddot{u}_i \quad \text{in } \Omega \quad (\text{Eqn-4}).$$

For 2D anti-plane deformation, displacement at any point (x, y) , and time t , is $u_z(x, y, t)$. Corresponding stress components are σ_{xz} and σ_{yz} . Eqn-4 gives wave equation for linear elastic homogeneous material with infinitesimal strain approximation. Slow deformation during interseismic period allows ignoring inertia term and solving a series of static equilibria with tectonic plate deformation and friction boundary condition on the fault surface. Ignoring body force (b_i) and dropping inertia term ($\rho\ddot{u}_i$) Eqn-4 reduces to

$$\frac{\partial \sigma_{xz}}{\partial x} + \frac{\partial \sigma_{yz}}{\partial y} = 0 \quad (\text{Eqn-5}).$$

Slip constraint on the frictional interface at $y = 0$ is given by

$$u_z(x, 0^+, t) - u_z(x, 0^-, t) = d(x, t) \quad (\text{Eqn-6}).$$

Continuity of traction across the fault plane leads to

$$\sigma_{yz}(x, 0^+, t) = \sigma_{yz}(x, 0^-, t) = T^f \quad (\text{Eqn-7}).$$

For elastoplastic bulk, constitutive relation with additive decomposition of total strain gives

$$\dot{\sigma}_{xz} = 2\mu (\dot{\epsilon}_{xz} - \dot{\epsilon}_{xz}^p), \quad \text{and} \quad \dot{\sigma}_{yz} = 2\mu (\dot{\epsilon}_{yz} - \dot{\epsilon}_{yz}^p) \quad (\text{Eqn-8}).$$

where, μ is the shear modulus and components of the symmetric total strain tensor are given by

$$\epsilon_{xz} = \frac{1}{2} \frac{\partial u_z}{\partial x}, \quad \text{and} \quad \epsilon_{yz} = \frac{1}{2} \frac{\partial u_z}{\partial y} \quad (\text{Eqn-9}).$$

We use J2 plasticity model to capture the inelastic response of the off-fault bulk. For 2D anti-plane problem, it reduces to a yield function:

$$F(\sigma) = \sqrt{(\sigma_{xz}^2 + \sigma_{yz}^2)} - \sigma_y \quad (\text{Eqn-10}).$$

Where, σ_y is the bulk yield strength. Plastic strain rate is expressed as,

$$\dot{\epsilon}_{xz}^p = \dot{\gamma} \frac{\partial F}{\partial \sigma_{xz}}, \quad \text{and} \quad \dot{\epsilon}_{yz}^p = \dot{\gamma} \frac{\partial F}{\partial \sigma_{yz}} \quad (\text{Eqn-11}).$$

Where, $\dot{\gamma}$ is the consistency parameter defining the rate of equivalent plastic strain. We use a radial return mapping algorithm (Simo & Hughes, 2006; Abdelmeguid & Elbanna, 2022b) to update the stresses.

In earthquake cycle simulation, the above equations need to be solved for an effectively unbounded domain. Spectral boundary integral enables truncating the computational domain by replacing the exterior homogeneous linear elastic half spaces with integral relation between the shear stress and displacement history (Breitenfeld & Geubelle, 1998; Geubelle & Breitenfeld, 1997; Geubelle & Rice, 1995; Lapusta et al., 2000; Abdelmeguid et al., 2019; Abdelmeguid & Elbanna 2022a, 2022b). For 2D antiplane problem, the shear stress at the boundary of the homogeneous half space is given by

$$T_3^{s\pm}(x, t) = T_3^o{}^{s\pm}(x, t) \mp \frac{\mu}{c_s} \dot{u}_3^\pm(x, t) + f_3^\pm(x, t) \quad (\text{Eqn-12}).$$

Where, the superscripts +, and - indicate top and bottom half space respectively. T_3^o represents the initial stress as well as any externally applied stress. \dot{u}_3 represent particle velocity and c_s is shear wave speed. f_3 is a functional resulting from space-time convolution of the displacement history at the boundary expressed in Fourier domain. In the velocity representation, the Fourier coefficient of $f_3^\pm(x, t)$ is expressed as

$$F_3^\pm(t; k_n) = \mp \mu |k_n| U_3^\pm(t; k_n) \pm \int_0^t W_{33}(|k_n| c_s t') \dot{U}_3^\pm(t - t'; k_n) dt' \quad (\text{Eqn-13}).$$

The convolution kernel is given by $W_{33}(\xi) = \int_\xi^\infty \frac{J_1(\zeta)}{\zeta} d\zeta$, where $J_1(\zeta)$ is the order one Bessel function of the first kind. Wave number, $k_n = 2\pi n/\lambda$, with replication length λ . U_3 and \dot{U}_3 are the Fourier coefficients of displacement and velocity respectively. For the

aseismic slow deformation phase, the velocity terms from Eqn-12 and Eqn-13 can be neglected. The first term in Eqn-13 represents the static contribution,

$$\tilde{F}_3^\pm(t; k_n) = \mp \mu |k_n| U_3^\pm(t; k_n) \quad (\text{Eqn-14}).$$

Also considering the stress increment beyond the initial condition, we can set $T_3^{s\pm} = 0$.

Therefore, the boundary stress, $T_3^{s\pm}(x, t)$ can be calculated using inverse Fourier transform of $\tilde{F}_3^\pm(t; k_n)$.

We incorporate the fault surface in FEM using domain decomposition technique (Aagaard et al., 2013), where the Lagrange multiplier represents fault traction (T^f). Weak form of the governing equation gives following system of equations (Abdelmeguid et al., 2019; Abdelmeguid & Elbanna, 2022b):

$$\mathbf{K}u - F^p + \mathbf{L}_f^T T^f + \mathbf{L}_s^T T^s = F \quad (\text{Eqn-15})$$

$$\mathbf{L}_f u = \mathbf{L}_d d \quad (\text{Eqn-16}).$$

For elastoplastic bulk, plastic force is obtained by integrating the plastic strain, $F^p = \int_{\Omega} \mathbf{B}^T \mathbf{D} \epsilon^p d\Omega$. Where, \mathbf{B} is the strain-displacement matrix, \mathbf{D} is the matrix with material moduli. \mathbf{K} denotes the stiffness matrix; F is the force vector. \mathbf{L}_f , \mathbf{L}_d and \mathbf{L}_s is comes from integrating the shape function.

We use a predictor-corrector approach to solve for the unknown displacements and fault tractions. Fault slip rate is then calculated from the following equation by equating fault total traction with fault strength and including radiation damping approximation for inertia (called quasi-dynamics approach). With radiation damping coefficient, $\eta_r = \frac{\mu}{2c_s}$,

$$T^f + T_o^f = \sigma_e f(V, \theta) + \frac{\mu V}{2c_s} \quad (\text{Eqn-17}).$$

Where, T_o^f is fault initial traction. Slip for next time step is computed by integrating the slip rate.

Solution steps for Quasi-dynamics solver:

1. At any time, t , for given slip, $d(t)$, state variable, $\theta(t)$, applied tectonic deformation, $u_b(t) = V_p t$, displacement $u(t - \Delta t)$, plastic strain, $\epsilon^p(t - \Delta t)$ and hence plastic force, $F^p(t - \Delta t) = \int_{\Omega} \mathbf{B}^T \mathbf{D} \epsilon^p(t - \Delta t) d\Omega$ are known.
2. Prediction for SBI boundary traction, T^s , using $u(t - \Delta t)$.
3. Elastic predictor step, $F^p(t) = F^p(t - \Delta t)$.
4. Solve linear system of equations for $u(t)$ and $T^f(t)$:

$$\mathbf{K}u - F^p + \mathbf{L}_f^T T^f + \mathbf{L}_s^T T^s = F$$

$$\mathbf{L}_f u = \mathbf{L}_d d$$

5. Corrector for SBI boundary traction using $\frac{1}{2}[u(t) + u(t - \Delta t)]$.
6. Plastic corrector: using radial return algorithm, compute $\epsilon^p(t)$ and $F^p(t)$.
7. Repeat steps 4 – 6 until error, $\frac{\|u^{n+1}(t) - u^n(t)\|}{\|u^{n+1}(t)\|} < tolerance$
8. Compute slip rate, V , using T^f from: $T^f + T_o^f = \sigma_e f(V, \theta) + \frac{\mu V}{2c_s}$
9. Estimate time increment based on slip rate and characteristic slip distance,

$$\Delta t = \min [C \frac{L}{V}] \quad (\text{Lapusta et al., 2000})$$

10. Update slip and state variable for next time step:

$$d(t + \Delta t) = d(t) + V(t)\Delta t$$

$$\dot{\theta}(t) = 1 - V(t) \theta(t)/L$$

$$\theta(t + \Delta t) = \theta(t) + \dot{\theta}(t)\Delta t$$

Fully dynamics solver with coupling of finite element and spectral boundary integral scheme is outlined in our previous studies (Mia et al., 2022; Abdelmeguid & Elbanna, 2022a, 2022b).

Table S1. List of parameters used in the simulations.

Parameter	Symbol	Values
Effective normal stress on fault	σ_n	50 MPa
Critical slip distance	L	500×10^{-6} m
Plate rate	V_p	10^{-9} m/s
Reference Slip rate	V_0	10^{-6} m/s
Initial slip rate	V_{init}	10^{-9} m/s
Reference friction coefficient	f_0	0.6
Shear wave speed	c_s	3464 m/s
Shear modulus	μ	32.038 GPa
Yield strength	σ_y	Variable
Nucleation length	L_{nuc}	100 m
Process zone size	R	21.36 m
Mesh size	dx and dy	0.5 m

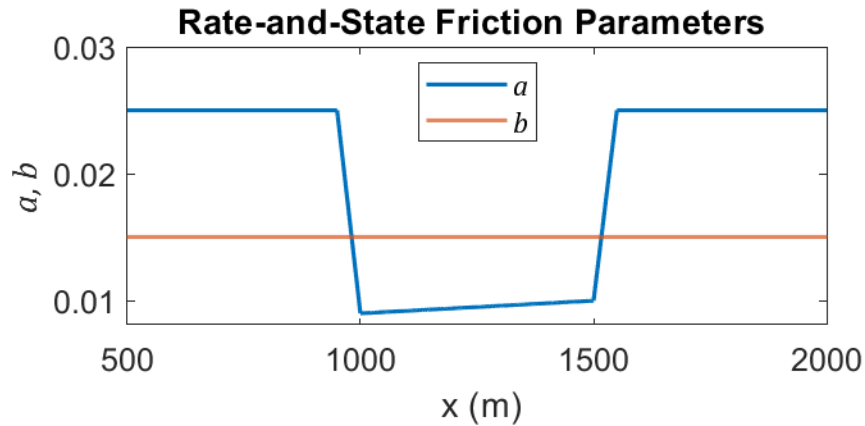
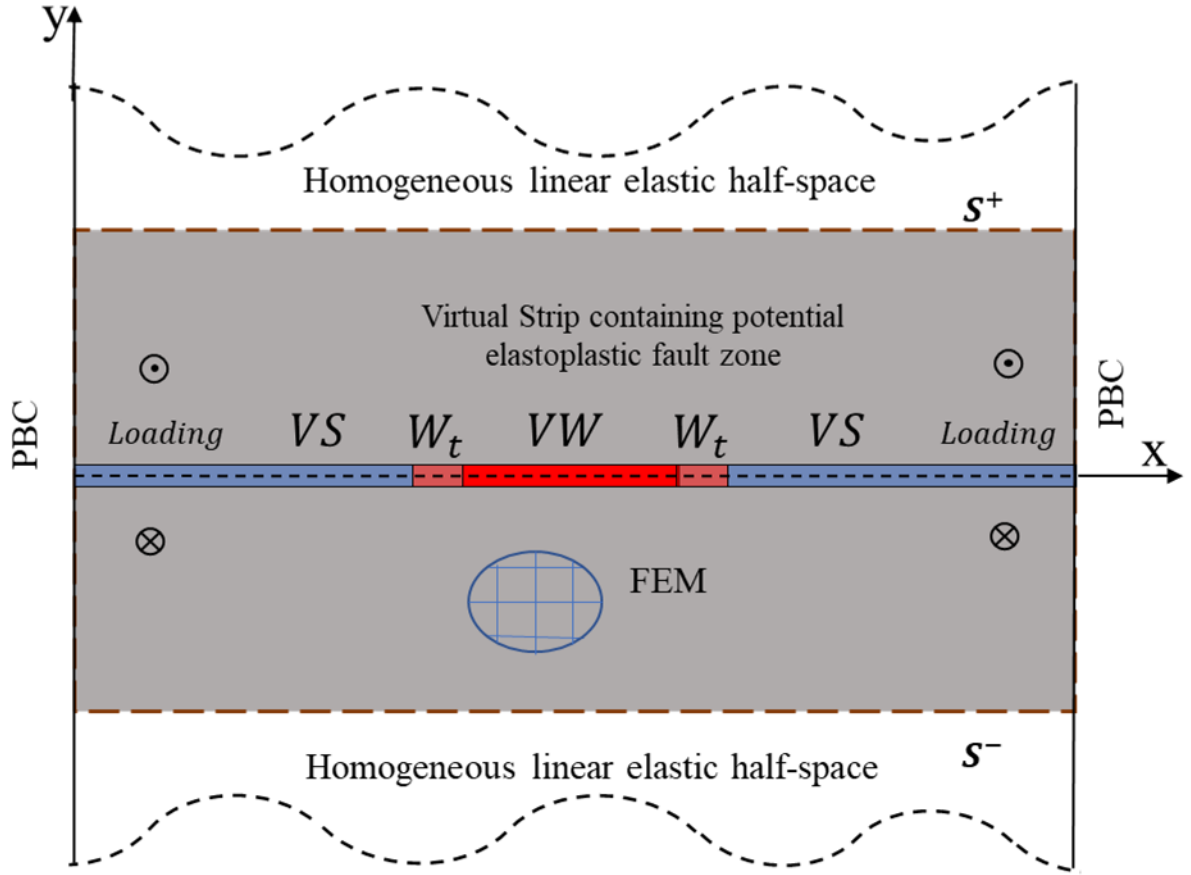


Figure S1. Model geometry and hybrid scheme set-up (Mia et al., 2019). 2D anti-plane rate-and-state fault contains seismogenic velocity weakening (VW) patch and creeping velocity strengthening (VS) patch with a transition region (W_t). Tectonic plate loading is applied through out of plane constant slip rate, $V_p = 10^{-9}$ m/s. Narrow virtual strip containing fault and potential elastoplastic bulk is discretized with FEM. Spectral Boundary Integral (SBI) replaces homogeneous linear elastic half spaces at the virtual boundaries (S^+ and S^-). Periodic Boundary Conditions (PBC) are applied at the lateral boundaries. Bottom figure shows the distribution of rate-and-state frictional parameters. a and b are non-negative dimensionless rate-and-state frictional parameters related to direct effect and state evolution respectively. Velocity weakening (VW) patch is associated with $a < b$ and velocity strengthening (VS) refers to $a > b$.

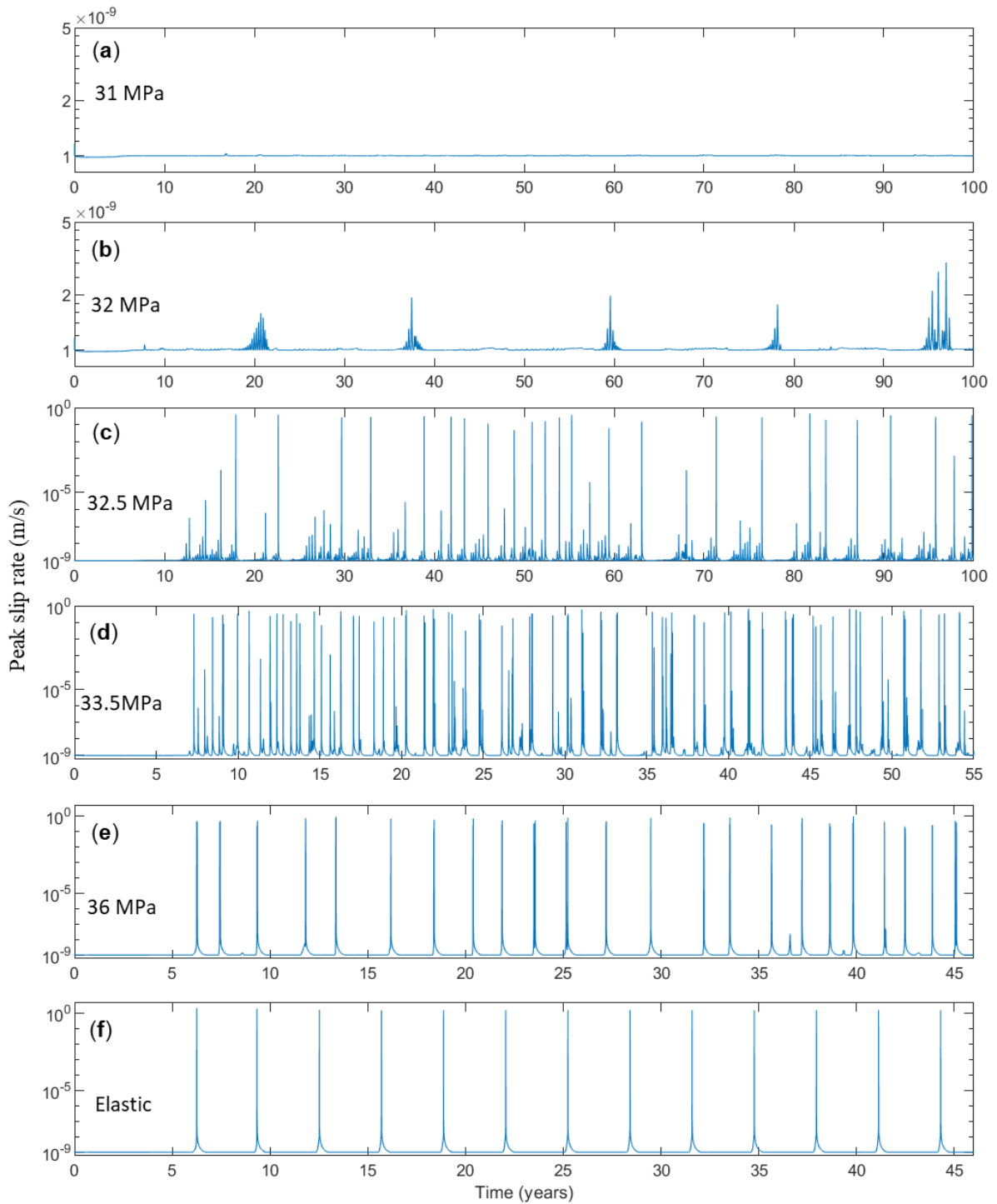


Figure S2. History of peak slip rate for different yield strength (a-e). Elastic reference case is generating periodic pattern is shown in f. Peak slip rate remains close to the plate rate for locked fault with yield strength 31 MPa as shown in a. (b) Slow slip events with 32 MPa. (c) Localized seismic events and preceding slow slip events with 32.5 MPa. (d) Irregular pattern including slow slip and partial rupture with 33.5 MPa. (e) Aperiodic sequence with clustering of seismicity for higher yield strength.

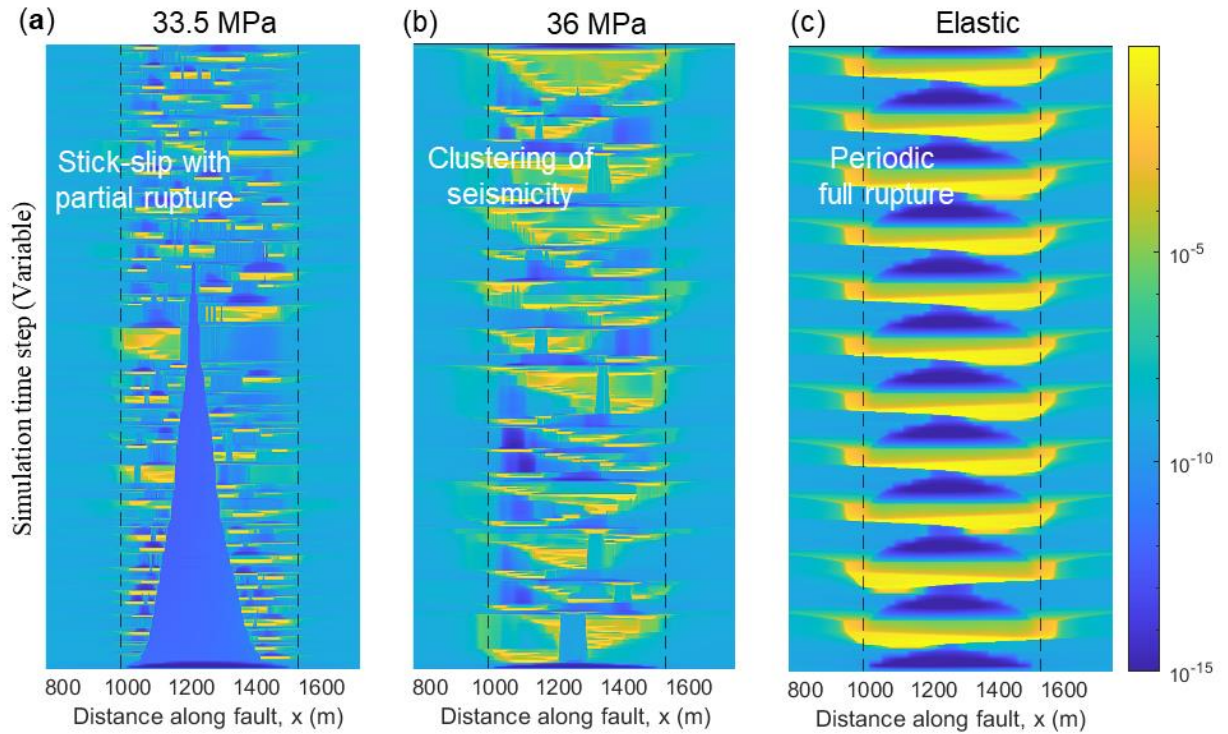


Figure S3. Results of fully dynamics simulation illustrating spatio-temporal evolution of slip rate. Patterns are qualitatively similar to the corresponding quasi-dynamics cases discussed in the main text. **(a)** Yield strength 33.5 MPa results in partial ruptures successively unlock the central VW region and spread over the whole fault. **(b)** Relatively higher yield strength (36 MPa) shows clustering of seismicity. **(c)** Elastic case generates simple periodic fault spanning ruptures.

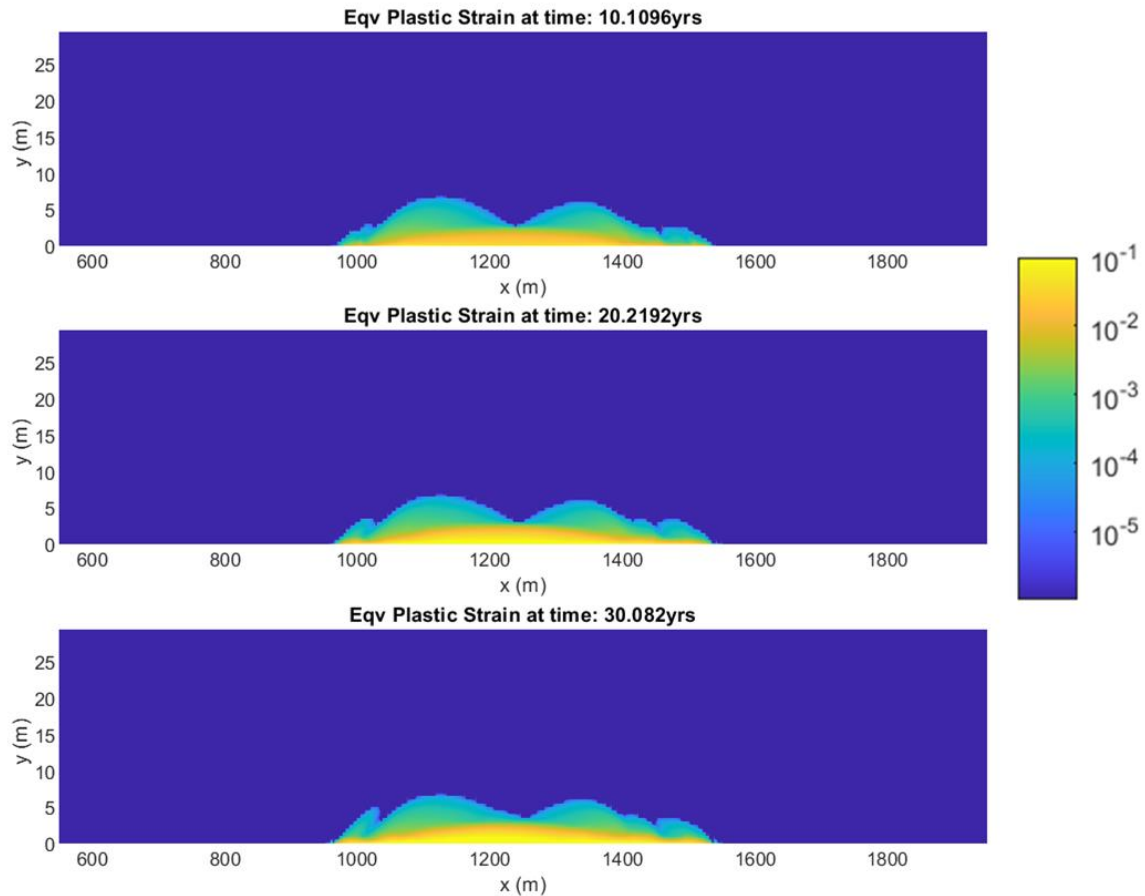


Figure S4. Equivalent plastic strain for yield strength 33.5 MPa. Spatial extent of off-fault plasticity perpendicular to the fault plane is limited to narrow region close to the fault. Plasticity distribution is symmetric across the fault plane as the model is anti-plane with constant normal stress. Horizontally, plasticity spreads along whole VW region of the fault.

References

- Aagaard, B. T., Knepley, M. G., & Williams, C. A. (2013). A domain decomposition approach to implementing fault slip in finite-element models of quasi-static and dynamic crustal deformation. *Journal of Geophysical Research: Solid Earth*, 118(6), 3059–3079. <https://doi.org/10.1002/jgrb.50217>
- Abdelmeguid, M., Ma, X., & Elbanna, A. (2019). A Novel Hybrid Finite Element-Spectral Boundary Integral Scheme for Modeling Earthquake Cycles: Application to Rate and State Faults With Low-Velocity Zones. *Journal of Geophysical Research: Solid Earth*, 124(12), 12854–12881. <https://doi.org/10.1029/2019JB018036>
- Abdelmeguid, M., & Elbanna, A. (2022a). Sequences of seismic and aseismic slip on bimaterial faults show dominant rupture asymmetry and potential for elevated seismic hazard. *Earth and Planetary Science Letters*, 593. <https://doi.org/10.1016/j.epsl.2022.117648>

- Abdelmeguid, M., & Elbanna, A. (2022b). Modeling Sequences of Earthquakes and Aseismic Slip (SEAS) in Elasto-Plastic Fault Zones With a Hybrid Finite Element Spectral Boundary Integral Scheme. *Journal of Geophysical Research: Solid Earth*, 127(12). <https://doi.org/10.1029/2022JB024548>
- Ben-Zion, Y., & Rice, J. R. (1997). Dynamic simulations of slip on a smooth fault in an elastic solid. *Journal of Geophysical Research: Solid Earth*, 102(B8), 17771-17784.
- Breitenfeld, M. S., & Geubelle, P. H. (1998). Numerical analysis of dynamic debonding under 2D in-plane and 3D loading. *International Journal of Fracture*, 93(1), 13-38.
- Dieterich, J. H. (1979). Modeling of rock friction: 1. Experimental results and constitutive equations. *Journal of Geophysical Research: Solid Earth*, 84(B5), 2161-2168.
- Geubelle, P. H., & Breitenfeld, M. S. (1997). Numerical analysis of dynamic debonding under anti-plane shear loading. *International Journal of Fracture*, 85(3), 265-282.
- Geubelle, P. H., & Rice, J. R. (1995). A spectral method for three-dimensional elastodynamic fracture problems. *Journal of the Mechanics and Physics of Solids*, 43(11), 1791-1824.
- Lapusta, N., Rice, J. R., Ben-Zion, Y., & Zheng, G. (2000). Elastodynamic analysis for slow tectonic loading with spontaneous rupture episodes on faults with rate-and state-dependent friction. *Journal of Geophysical Research: Solid Earth*, 105(B10), 23765-23789.
- Mia, M. S., Abdelmeguid, M., & Elbanna, A. E. (2022). Spatio-Temporal Clustering of Seismicity Enabled by Off-Fault Plasticity. *Geophysical Research Letters*, 49(8). <https://doi.org/10.1029/2021GL097601>
- Ranjith, K., & Rice, J. R. (1999). Stability of quasi-static slip in a single degree of freedom elastic system with rate and state dependent friction. *Journal of the Mechanics and Physics of Solids*, 47(6), 1207-1218.
- Rice, J. R. (1993). Spatio-temporal complexity of slip on a fault. *Journal of Geophysical Research: Solid Earth*, 98(B6), 9885-9907.
- Rubin, A. M., & Ampuero, J. P. (2005). Earthquake nucleation on (aging) rate and state faults. *Journal of Geophysical Research: Solid Earth*, 110(B11), 94-144.
- Ruina, A. (1983). Slip instability and state variable friction laws. *Journal of Geophysical Research: Solid Earth*, 88(B12), 10359-10370.
- Simo, J. C., & Hughes, T. J. (2006). *Computational inelasticity* (Vol. 7). Springer Science & Business Media.